Analysis and Prediction of Edge Effects in Laser Bending

Jiangcheng Bao and Y. Lawrence Yao*
Department of Mechanical Engineering, Columbia University
New York, NY 10027, USA

*Corresponding author, Tel: (212) 854-2887, Fax: (212) 854-3304, email: YLY1@columbia.edu

Abstract

In single-axis laser bending of plates, the bending edge is found to be somewhat curved and the bending angle varies along the laser-scanning path. These phenomena are termed edge effects, which adversely affect the accuracy of the bending and result in undue residual stress. Numerical and experimental investigations are carried out to study the process transiency and the mechanism of the edge effects. Patterns of edge effects and resultant residual stress distributions are examined under a wide range of conditions corresponding to different forming mechanisms. A more complete explanation for the mechanism of the edge effects is given.

1. Introduction

Most research work to date has been focused on straight-line laser bending, a simple form of laser forming. A simple beam model was proposed based on the temperature gradient mechanicsm (TGM) assumption and an energy approach to the temperature field was used in a two-layer model (Vollertsen, 1994). Mucha, et al. (1997) modeled the TGM and provided solutions, by assuming different shaped plastic zones. This model helped determine the critical conditions for the TGM. By assuming a complete plastic zone in the area near the center of the beam, and a complete elastic zone in remote areas, Vollertsen, et al. (1995) established an analytical model for the buckling (BM). This model is valid for high ratio of thermal conductivity to thickness, i.e., the heat conduction is basically 2D. Alberti, et al. (1994) carried out a numerical simulation of the laser bending process by a thermal mechanical analysis. Hsiao, et al. (1997) simulated the bending process and used extrapolation for mechanical properties at higher temperature. Holzer, et al. (1994) modeled the bending process under BM. As temperature often rises very high in laser forming, temperature dependency of material properties becomes very important to the simulation accuracy. Large deformation is desired in laser forming, and consequently, it is necessary to consider strain hardening, especially in the case of multiple scan (Sprenger, et al., 1994). In order to obtain higher productivity, high travelling velocities are often employed in laser forming. In such cases, the strain rate could be high. Dependency of flow stress on the strain rate is much stronger at elevated temperatures (Li & Yao, 1999).

Despite of the progress made to date, there still exist problems that need to be addressed. Among them are the geometrical accuracy and residual stress of laser formed components. In the straight-line laser bending, variation of the bending angle along the bending edge has been observed, as illustrated in Fig. 1. The bending edge is also somewhat curved. These two forms of inaccuracies together are termed as edge effects in this paper. The edge effects are obviously undesirable since they cause the deviation from the design intent (constant bending angle along

the straight bending edge), cause a certain warpage of the component, and may cause additional residual stresses.

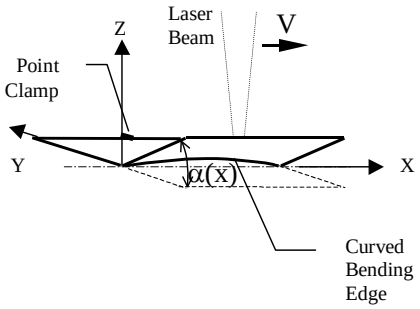

Fig. 1 Straight-line laser bending showing edge effects characterized by the curved bending edge and non-uniform bending angle $\alpha(x)$

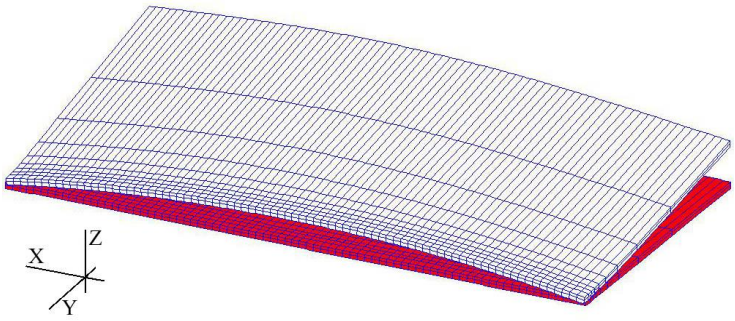

Fig. 2 Deformed compared with undeformed plate, deformation magnification 5X, half plate of 80 x 80 x 0.89 mm^3, V=26.7 mm/s, P=800 W, beam diameter=8 mm, AISI 1010, time=1,000 sec.

Magee, et al., (1997) showed that the extent of edge effects depends on the thermal diffusion from the laser beam into the entire plate, and the geometrical constraint of the workpiece as it varies with distance from the end point of the scanning path. The actual profile of bending angle is dependent on the laser processing parameters employed, as well as the material properties. Materials with very different thermal conductivity and expansion exhibited different variation patterns of the bending angle. Attempts have been made to reduce the edge effects by empirically varying the traveling velocity along the scanning path. Results showed that the varying velocity profile could lead to a sizable reduction of the edge effects.

Theoretical analysis by Mucha et al. (1997) showed that thickness in the bending edge region increases due to thermal contraction under the TGM, and the bending edge of the plate is visibly curved due to thermal contraction in the scanning direction. Again, this analytical model does not describe the transient stage, while understanding of the transient stage is useful in analyzing the causes of the edge effects and realizing process control.

This paper presents experimental and numerical investigations aimed at advancing the understanding of the causes of the edge effects in the straight-line laser bending process under a wide range of conditions. These conditions correspond to different forming mechanisms. Experimental results provide more laser forming data under different conditions and are used to validate the numerical results. Numerical results provide more insights into the causes of the edge effects, and help predict such effects on final dimensional accuracy and residual stress.

2. Numerical Simulation

The following assumptions are made for the numerical modeling. The power density distribution of the laser beam follows a Gaussian function. The laser operates in CW mode. No cooling gas or water jet is employed. Dissipation of energy due to plastic deformation is negligible compared with the intensive energy involved. It is assumed that no melting is involved in the forming process.

Temperature dependency of material properties is considered, including thermal conductivity, specific heat, Young's modulus, Poisson ratio, and flow stress. Elastic strains are assumed to be much smaller than unity. Strain hardening of the material is considered through the strain-hardening coefficient, which is also temperature dependent. Dependency of flow stress on strain

rate is modeled by defining a stress ratio $R(\theta, \dot{\varepsilon})$, the ratio of the flow stress at a certain strain rate to the static flow stress, as a function of temperature θ and strain rate $\dot{\varepsilon}$.

Since the heat transfer and elastic/plastic deformation are symmetric about the vertical plane containing the scanning path, only half of the plate is modeled in the numerical simulation. The same mesh model is used for the heat transfer analysis and structural analysis. In order to capture high gradients of temperature near the scanning path, a fine mesh is used in that region, while a coarse one in remote areas.

A commercial code, ABAQUS, is used for the thermal mechanical simulation, employing a sequentially coupled heat transfer and structural analysis. In the structural analysis, the twenty-node element, C3D20, has no shear locking or hourglass effect, and is thus suitable for a bending-deformation-dominated process such as laser forming. On the other hand, the eight-node element suffers from "shear locking", and is therefore not suitable for such a process. In order to keep compatible with the structural analysis, a twenty-node element, DC3D20, is used in the heat transfer analysis.

Laser beam is given as prescribed nonuniform surface heat flux: $q = q(x, y, t)$ on the top surface. On five of the six boundary surfaces (except for the symmetric plane), free convection with air is considered: $q = h\,(\theta - \theta_0)$, where h is the heat transfer coefficient, and $\theta_0 = \theta_0\,(x, t)$ the surrounding temperature. Radiation is also considered on these five surfaces: $q = A\,((\theta - \theta_Z)^4 - (\theta_0 - \theta_Z)^4)$, where A is the radiation constant, and θ_Z the absolute zero on the temperature scale used. The symmetric plane is assumed to be adiabatic.

Two adjacent points in the middle of the symmetric plane are fixed in order to remove the rigid body motion. All other points within the symmetric plane are assumed to move only within the symmetric plane throughout the deformation process.

3. Experiment

The laser system used in the experiment is a PRC-1500 CO_2 laser, with a maximum output power of 1500 W. A coordinate measuring machine (CMM) is used to measure the bending angle at different positions along the scanning path. Coordinates of different points along the scanning edge are also measured, and the curvature of the scanning edge is subsequently calculated from these coordinates. The flatness of the unbent plates is measured using the CMM and the non-uniformity is smaller as compared with the final bending angle. A point clamp is used in the middle of one side of a workpiece (Fig. 1). Using the point clamp, one can better focus on the mechanism of the edge effects internal to the workpiece.

The experiment conditions are shown in Table 1. Material is low carbon steel, AISI 1010. To enhance laser absorption by the workpiece, graphite coating is applied.

Table 1 Experimental conditions

Condition No.	Line Energy (J/mm)	Power (W)	Velocity (mm/s)	Sheet Size (mm^3)	Beam diameter (mm)
1	20	200 – 1300	10 – 67.5	80 x 80 x 0.60	8
2	20	200 – 1300	10 – 67.5	80 x 80 x 0.89	8
3	30	200 – 1300	10 – 45	80 x 80 x 0.89	8
4	30	400-1000	13.3 – 33.3	80 x 76.3 x 1.5	8
5	30	800-1300	40 – 65	80 x 76.3 x 2.3	4

By holding the line energy constant, the input energy per unit length along the scanning direction is kept unchanged even power and velocity change. Under conditions 1 to 3, the

bucking mechanism (BM) is likely to dominate because of the large beam diameter to sheet thickness ratio. Under condition 5, the temperature gradient mechanism (TGM) is more likely to dominate because of the smaller beam-diameter to thickness ratio.

4. Results and Discussion

Experimental and numerical results under conditions 1 to 3 exhibit very similar trends and therefore only results under condition 3 are presented and analyzed in details. First, simulation results are validated by experimental measurements. Additional simulation results are then presented to help understand the process transiency and underlying mechanism of the edge effects. Finally, they are briefly compared with results under conditions 4 and 5.

4.1 Comparison of experimental and simulation results

Fig. 2 shows a typical thermal-mechanical simulation result (deformation magnified for easier visualization). Due to symmetry only half plate is simulated. It takes about three seconds to scan the 80-mm path at the velocity used, while deformation does not complete till much later. A curved bending edge is seen at 1,000 seconds. Fig. 3 shows both experimental and simulation results of the bending angle along the scanning path and they agree each other quite well. It can be seen that, from the entering end of the scanning path (X = 0), the bending angle either drops a little and then increases or directly increases towards the exiting end, where the maximum value occurs.

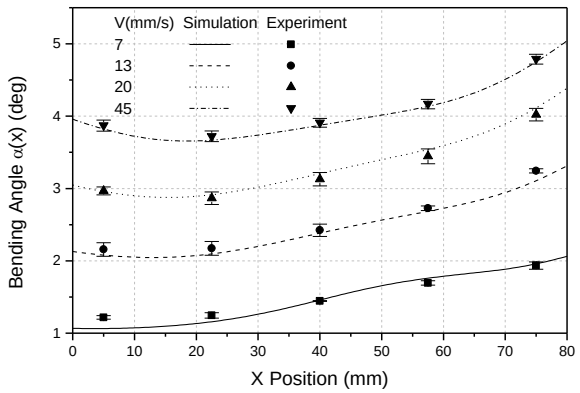

Fig. 3 Bending angle variation along the scanning path, $\alpha(x)$ (Condition 3)

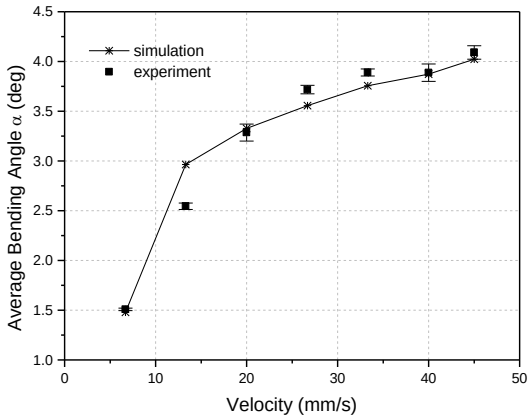

Fig. 4a Average bending angle (Condition 3)

Fig. 4 (a) shows the average bending angle vs. velocity. It can be seen that, despite the fact that the line energy is held constant, the average bending angle increases with velocity. Shown in Fig. 4 (b) is the curvature of the bending edge vs. velocity. Fig. 4 (c) shows comparison of experimental and numerical results of bending angle variation. The bending angle variation is defined as the difference between the maximal and minimal bending angle along the bending edge for a given condition.

Generally speaking, the simulation results agree quite well with the experimental results. Not only the average bending angle and curvature, but also the bending angle variations along the scanning direction are relatively well captured by the numerical model. As mentioned before, the

bending angle variation (Fig. 4 (c)) and curved bending edge (Fig. 4 (b)) together are termed edge effects in this paper. Similar results are obtained under conditions 1 and 2.

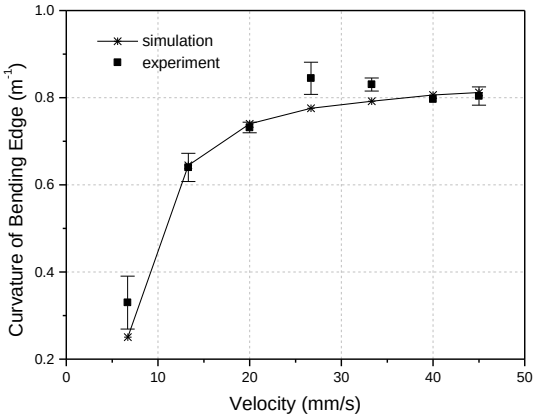

Fig. 4b Curvature of the bending edge (Condition 3)

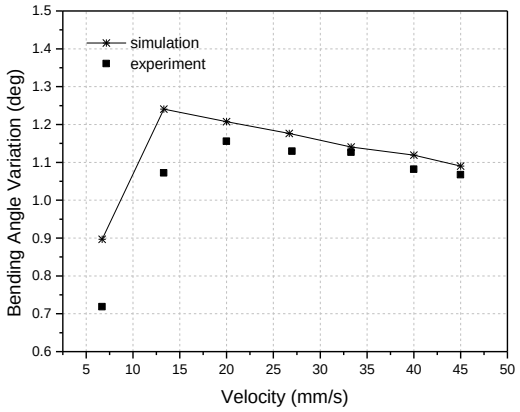

Fig. 4c Bending angle variation (difference between the max and min) (Condition 3)

4.2 Edge effects

To help understand the causes of the edge effects as seen in Figs. 3 and 4, additional numerical results are shown in Fig. 5 through Fig. 7. The peak temperature that points on the top surface along the scanning path typically experience is shown in Fig. 5 (a). Apparently, the much higher peak temperature at the exiting end is attributed to the reduced heat dissipation near the exit boundary. Fig. 5 (b) is a typical time history of temperature at the top and bottom surfaces along the scanning path for two different scanning velocities but at the same line energy. As seen, temperatures are higher at the higher velocity due to less time for heat dissipation. At the higher velocity, the difference between the peak temperature at the top and bottom surfaces is also larger than that at the lower velocity for the same reason.

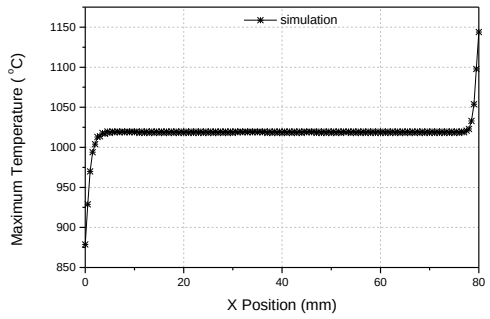

(a)

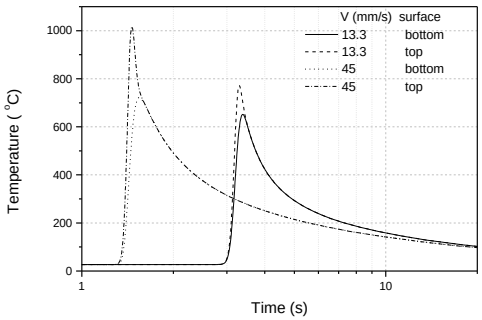

(b)

Fig. 5 (a) Typical peak temperature reached on the top surface along the scanning path (Condition 3, V = 45 mm/s), and (b) temperature history of a typical point on the scanning path (Condition 3, V = 13.3 and 45 mm/s)

Despite the fact that the line energy is held constant, the average bending angle increases with velocity (Fig. 4 (a)). This is mainly due to the fact that, at higher velocities, temperatures are higher because of less energy dissipation and temperature difference between the top and bottom surfaces is greater (Fig. 5 (b)). The fact that the temperature at the exit point is much higher than that at the entrance point (Fig. 5 (a)) explains why the bending angle at the exit point differs from that at the entrance point (Fig. 3). This is one reason why the bending angle is not uniform along

the scanning direction. The other cause for the bending angle variation is the curved bending edge (Fig. 4 (b)), which will be explained below.

The bending angle variation (Fig. 4 (c)), defined as the difference between the maximal and minimal bending angle along the scanning direction for a given operation, rises quickly first, peaks at about 20 mm/s, and then levels off or slightly decreases with the increase of velocity. The curvature of the bending edge also starts to decrease in slope significantly at around 20 mm/s (Fig. 4 (b)). It therefore seems reasonable to conclude that the curved bending edge is another reason for the bending angle variation to occur along the scanning direction.

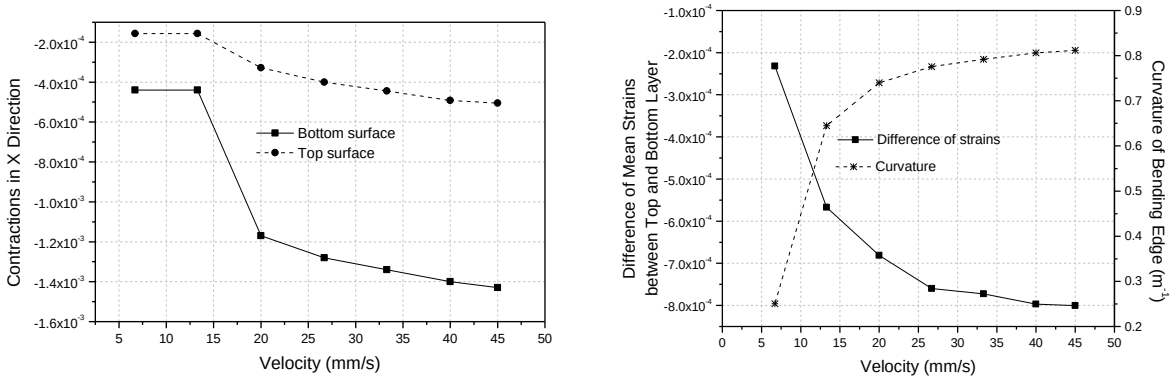

(a) (b)

Fig. 6 (a) Contractions in the scanning direction (X-axis), and (b) difference of mean strains between the top and bottom layer along the X-axis and curvature of the bending edge (Condition 3)

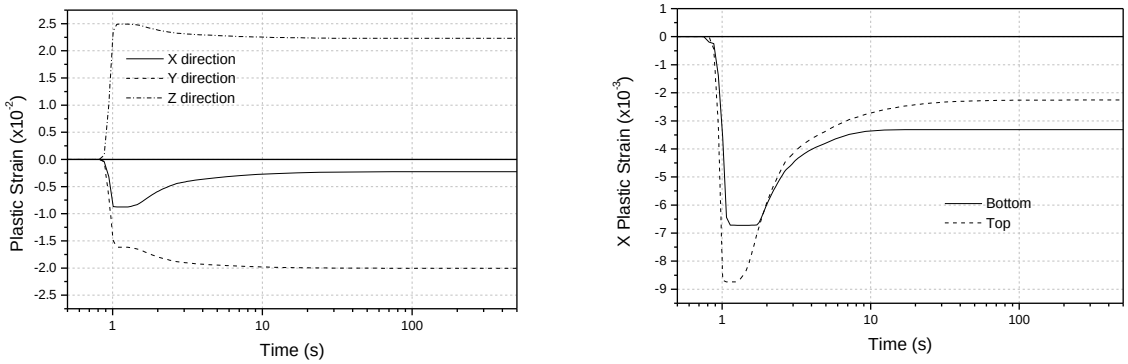

(a) (b)

Fig. 7 Time history of plastic strain for a typical point (X = 20 mm) (a) X-, Y-, and Z- axis plastic strain on the top surface along the scanning path, and (b) X-axis plastic strain on the top and bottom surfaces along the scanning path (Condition 3, V = 26.7 mm/s)

The cause of the curved bending edge is in turn due to the difference in the X-axis contraction between the top and bottom surfaces (Fig. 6). Fig. 6 (a) shows the simulation result of contractions in the X direction on the top and bottom surfaces along the scanning direction. Fig. 6 (b) shows the difference of the two contractions. The simulation result of the bending edge curvature in Fig. 4 (b) is also superposed here for the convenience of discussions. To further explain the X-axis contraction and the reason for the difference, the time history of plastic strains at a typical location on the scanning path (X = 20 mm) is examined in Fig. 7. Fig. 7 (a) shows the time history of the plastic strain on the top surface of that location (in three perpendicular directions). Fig. 7 (b) shows the time history of the X-axis plastic strain on the top and bottom

surfaces at the same location. Near the top layer along the scanning path, compressive strain occurs in the X and Y directions and tensile strain in Z direction (Fig. 7 (a)). Please note the sum of these plastic strains is zero at any given time based on the assumption of constant volume in plasticity (Mielnik, 1991), $d\varepsilon_1 + d\varepsilon_2 + d\varepsilon_3 = 0$, where ε_1, ε_2 and ε_3 are strains in three mutually perpendicular directions. During the rapid heating stage (at around one second seen in Fig. 7), a significant Y-axis compressive plastic strain occurs due to the great geometric constraint of the workpiece in that direction while the tensile plastic strain in the Z direction occurs freely due to the much less constraint in the thickness direction. Less well known is the compressive plastic strain in the X direction, which is also caused by the geometric constraint of the plate in that direction although the constraint is not as great as that in the Y direction. The bottom surface along the scanning path undergoes a very similar plastic deformation process as the top surface, except the magnitude is smaller. This is understandable because under condition 3, the buckling mechanism is dominant and thus the temperature difference between the top and bottom surface is moderate. A comparison between the plastic strains at the top and bottom surfaces is shown in Fig. 7 (b). Fig. 7(b) also shows that, during the cooling stage (after about one-second seen in Fig. 7), the reverse of the X-axis compressive plastic strain at the top surface is more than that at the bottom surface. This is because, during the cooling stage, the top surface undergoes more Y-axis compressive plastic strain (Fig. 7 (a)) than that at the bottom surface. Based on the constant volume assumption, the X-axis compressive plastic strain at the top surface reverses more than that at the bottom surface (Fig. 7 (b)). Therefore, the total X-axis contraction near the bottom layer is larger than that near the top layer (Fig. 6). Consequently, the bending edge is curved away from the laser beam (Figs. 1 and 2).

As seen in Fig. 6 (b), the greater is the difference between the contractions near the top and bottom surfaces, the greater the curvature. The fact that the curvature increases with velocity can be explained by the increase in average bending angle with velocity. Obviously, when the average bending angle is larger, the above-mentioned difference between the top and bottom surfaces will be more pronounced, and therefore the curvature will be greater. As seen from Figs. 4 (a) and (b), at higher velocities where the average angles are larger, the curvatures of the bending edge are also greater.

4.3 Residual stress

Residual stress affects such important materials design properties as fatigue life, fracture strength, and onset of yield. To study the residual stress, Fig. 8 shows a typical Y-axis plastic strain, elastic strain and residual stress distribution at the top, middle and bottom layers along the scanning path. As seen from Fig. 8, the plastic strain near both ends of the scanning path is small because the reduced geometric constraint of the plate in these regions, while along the rest of the scanning path significant compressive plastic strain is seen. This clearly explains why the residual stress is compressive at both ends and tensile along the rest of the scanning path.

It is worth to note that the difference in the plastic strain between the top and bottom surfaces at a location, say, X = 20 mm, is smaller than that at a location, say, X = 60 mm. This is because, before the laser beam reaches the location at X = 60 mm, a certain amount of compressive plastic strain near the top surface and tensile plastic strain near the bottom surface have already accumulated at the location due to the bending taking place at the preceding regions on the scanning path. This explains the bending angle at X = 20 mm is smaller than that at X = 60 mm (Fig. 3).

As seen in Fig. 8, the profile of the residual stress distribution is understandably very similar to that of the elastic strain distribution. The small shift along the vertical axis is governed by the relationship for isotropic elasticity, that is, $E_{22} = \frac{1}{E_Y}\left[T_{22} - \nu\left(T_{33} + T_{11}\right)\right]$, where E_{22} is the elastic strain in the Y direction, T_{11}, T_{22} and T_{33} are stress in the X, Y and Z direction, respectively. In this case, $T_{33} \approx 0$, and T_{11} is small as compared with T_{22}. Shown in Fig. 9 is the contour plot of the Y-axis residual stress along the scanning path and within the symmetric plane.

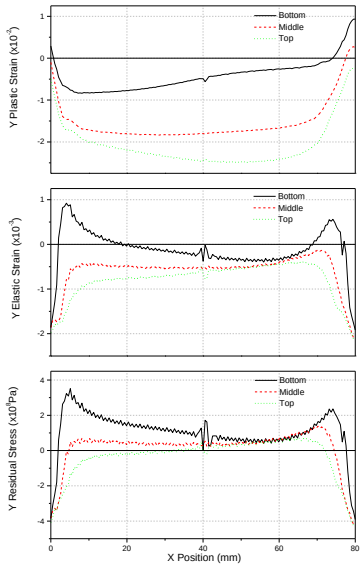

Fig. 8 Y-axis plastic strain, elastic strain and residual stress along the scanning path (Condition 3, V = 26.7 mm/s)

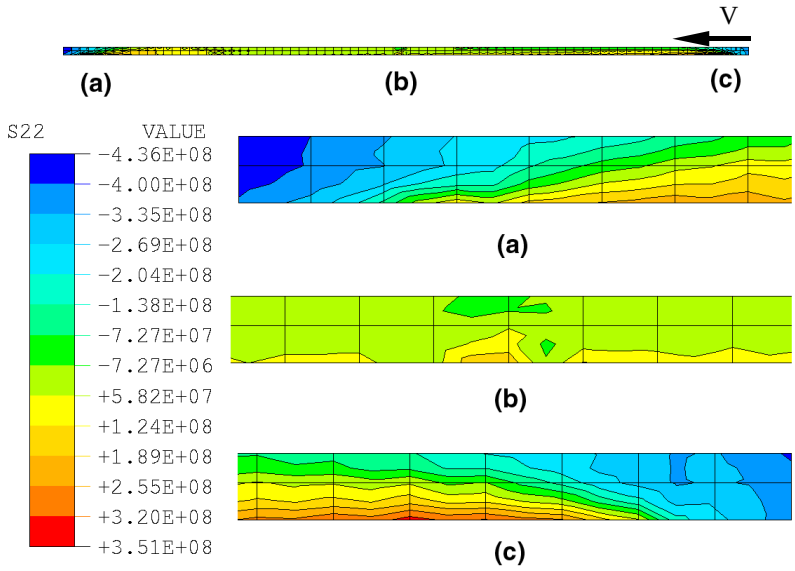

Fig. 9 Contour plot of Y-axis residual stress along the scanning path and within the symmetric plane (Condition 3, V = 26.7 mm/s)

4.4 Other conditions

So far, our discussion has been focused on condition 3 where the buckling mechanism (BM) of laser forming dominates. Under the condition, the edge effects are characterized by a concave bending angle variation (Fig. 3) and the scanning edge is curved away from the laser. Similar results are obtained in experiments and simulation under conditions 1 and 2. Under conditions 4 and 5, however, the BM may not dominate. In fact, under condition 5, the temperature gradient mechanism (TGM) dominates due to the reduced beam diameter and increased plate thickness. Condition 4 represents the situation where the BM transits to the TGM or the BM and TGM co-exist. As a result, the edge effects exhibit patterns different from condition 3. As seen from Fig. 10 (a), the bending angle variation measured along the scanning path is almost linear under condition 4. Experimental and simulation results show the bending angle variation is convex under condition 5 (Fig. 10 (b)). In addition, the scanning edge is curved towards the laser under condition 5 as opposed to curving away from the laser under condition 3.

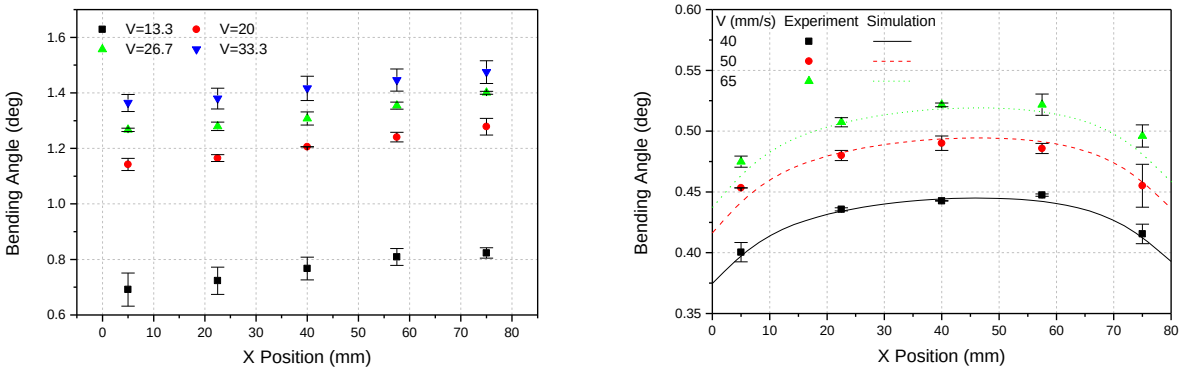

(a) (b)

Fig. 10 (a) Measurement of bending angle $\alpha(x)$ (Condition 4), and (b) simulation and experimental results of bending angle $\alpha(x)$ (Condition 5)

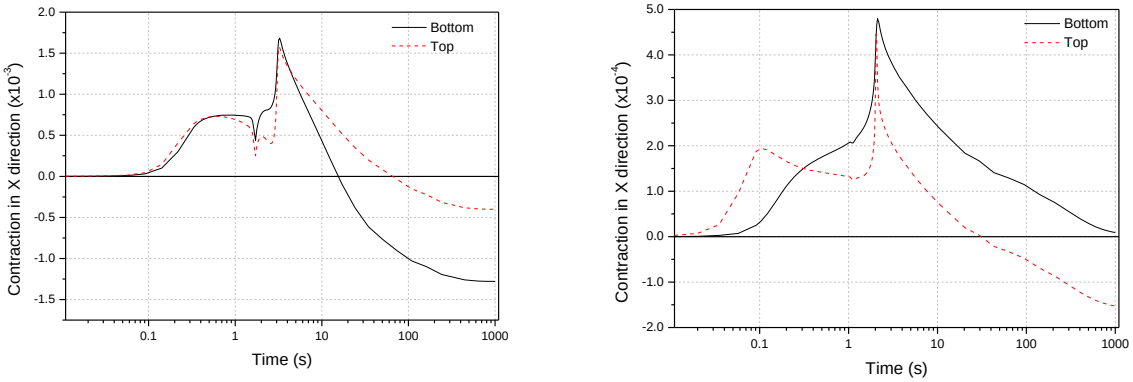

(a) (b)

Fig. 11 Time history of X-axis deformation (a) condition 3 (Buckling mechanism dominated), and (b) condition 5 (Temperate gradient mechanism dominated)

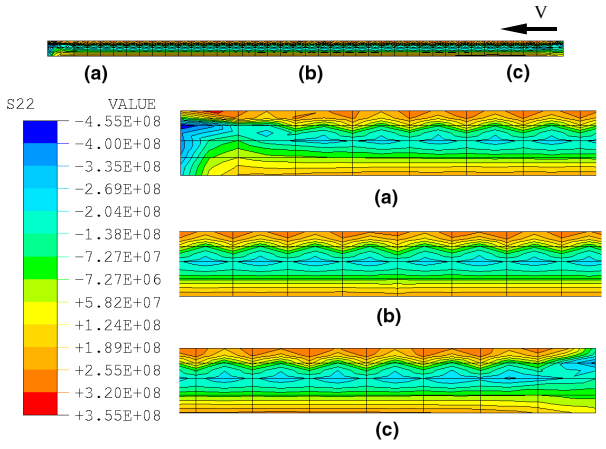

Fig. 12 Contour plot of Y-axis residual stress along the scanning path and within the symmetric plane (Condition 5, V = 26.7 mm/s)

The time history of the X-axis contraction for conditions 3 and 5 is plotted in Fig. 11. As seen from Fig. 11 (a), the top and bottom layers experience similar contraction during the heating stage for the BM-dominated bending operation (condition 3) where temperature difference between the top and bottom surfaces is moderate. But the bottom layer contracts more than the top layer during the cooling stage because the Y-axis contraction at the top surface is greater than that near the bottom surface. This leads to a bending edge curved away from the laser.

For the TGM-dominated bending operation where the temperature difference between the top and bottom layers is much greater (condition 5), the top layer contracts more than the bottom

layer during the cooling stage (Fig. 11 (b)) simply because the temperature gradient in the thickness direction is so dominant that it overwrites other effects. Shown in Fig. 12 is the contour plot of the Y-axis residual stress for condition 5. As seen, the top and bottom layers are tensile and the middle layer is compressive, which is typical for the TGM-dominated bending operation.

5. Conclusions

Both numerical and experimental results confirm that edge effects are characterized by a concave pattern in the bending angle variation along the scanning path and a bending edge curved away from the laser under conditions 1 to 3, where the forming process is dominated by the BM. Results from simulation and experiments also show that under condition 5 where the TGM dominates, the pattern of edge effects is different, which is characterized by a convex bending angle variation and the bending edge curved towards the laser.

In the case of the BM-dominated bending operation, the X-axis contraction near the bottom surface is more significant than that near the top surface, resulting a bending edge curved away form the laser, while the opposite is true in the case of the TGM-dominated bending process. Whether to obtain a convex or concave pattern of the bending angle variation is closely related with the direction of the curved bending edge.

References

Alberti, N., Fratini, L., Micari, F., "Numerical simulation of the laser bending process by a coupled thermal mechanical analysis," *Laser Assisted Net shape Engineering, Proceedings of the LANE'94*, Vol. 1, Meisenbach Bamberg, p327-336.

Holzer, S., Arnet, H., Geiger, M., "Physical and numerical modeling of the buckling mechanism," " *Laser Assisted Net shape Engineering, Proceedings of the LANE'94*, Vol. 1, Meisenbach Bamberg, p379-386.

Hsiao, Y.-C., Maher, W., et al., 1997, "Finite element modeling of laser forming," *Proc. ICALEO'97*, Section A, p31-40.

Li, W., Yao, Y. L., 1999, "Effects of strain rate in laser forming," *ICALEO '99*, San Diego, CA, Nov. 1999.

Magee, J., Watkins, K. G., Steen, W. M., 1998, "Advances in laser forming," *Journal of Laser Applications*, Vol. 10 n 6, p235-246.

Magee, J., Watkins, K. G., Steen, W. M., Calder, N., Sidhu, J. and Kirby, J., 1997, "Edge effects in laser forming," *Laser Assisted Net shape Engineering 2, Proceedings of the LANE'97*, Meisenbach Bamberg, p399-408.

Mielnik, E. M., 1991, Metalworking Science and Engineering, McGraw-Hill, Inc..

Mucha, Z., Hoffman, J., Kalita, W., Mucha, S., 1997, "Laser forming of Thick free plate," *Laser Assisted Net shape Engineering 2, Proceedings of the LANE'97*, Meisenbach Bamberg, p383-392.

Sprenger, A., Vollertsen, F., Steen, W. M., Waltkins, K., 1994, "Influence of Strain Hardening on Laser Bending," *Laser Assisted Net shape Engineering, Proceedings of the LANE'94*, Vol. 1, Meisenbach Bamberg, p361-370.

Vollertsen, F., 1994, "An analytical model for laser bending," *Lasers in Engineering*, Vol. 2, p261-276.

Vollertsen, F., Komel, I., Kals, R., 1995, "The laser bending of steel foils for microparts by the buckling mechanism -- a model," *Modeling and Simulation of Material Science and Engineering*, Vol. 3, p107-119.